



# Processing and modeling of 3D-printed mill scale strengthened acrylonitrile butadiene styrene composites

Jennarong Tungtrongpaioj<sup>1</sup> · Korbkaroon Doungkeaw<sup>1</sup> · Boonlom Thavornyutikarn<sup>2</sup> ·  
Peeraphat Suttipong<sup>1</sup> · Vitoon Uthaisangsuk<sup>3</sup>

Received: 21 October 2023 / Accepted: 12 January 2024 / Published online: 10 February 2024  
© The Author(s), under exclusive licence to Springer-Verlag London Ltd., part of Springer Nature 2024

## Abstract

Mill scale (MS) strengthened acrylonitrile-butadiene-styrene (ABS) composite filaments were fabricated as an optional low-cost and sustainable feedstock material with enhanced strength using fused filament fabrication (FFF) technology. In the present study, the effects of the FFF printing parameters on the mechanical properties of the printed ABS/1.0 vol% MS composites were evaluated. Test specimens of the composite were fabricated at printing temperatures of 240–280 °C, printing speeds of 10–90 mm s<sup>-1</sup>, and infill densities of 25–100%. Tensile tests and Izod impact tests were conducted for the specimens printed under different printing conditions to examine their mechanical characteristics. Afterwards, macro- and microstructural observations of the fractured specimens were carried out. The average maximum stress and modulus of the printed specimens increased when the printing temperature was raised to 270 °C while decreasing the printing speed, with numerous air gaps and pores found in the cross-sectional microstructures after failure at low infill density. High surface roughness of the printed composites was observed by a 3D laser scanner when printing at high temperatures and speeds due to insufficient cooling. The printed composite microstructures were examined by X-ray micro-computed tomography (μCT), and showed homogeneously dense particle dispersion in the entire printed part. Representative volume element (RVE)-based modeling was carried out using real particle geometries from the μCT. RVE simulations predicted high local stress distributions around mill scale particles and air gaps in the printed samples.

**Keywords** Thermoplastic filament · Recycling · Composite filament · Three-dimensional printing technology · Representative volume elements

## 1 Introduction

Additive manufacturing (AM), generally referred to as three-dimensional (3D) printing, has been used to produce many applications in the automotive, aerospace, defense, and biomedical industries instead of traditional manufacturing processes [1, 2]. The AM market size was forecast to quadruple between 2014 and 2021 [3, 4]. Fused filament fabrication (FFF) is an attractive 3D printing technology to generate and produce various 3D geometric objects. FFF is a rapid, cost-effective, and relatively simple operation for making complex parts [5–7]. Polymer matrix composite (PMC) filaments are widely used as raw materials, including thermoset composites (TSC), thermoplastic composite materials (TPC), and continuous fiber-reinforced polymer composites (CFRPC). Development of FFF filament feedstocks from these materials has attracted interest due to their inherent lightweight and high strength-to-weight ratio [8, 9].

✉ Jennarong Tungtrongpaioj  
jennarongt@eng.kmutnb.ac.th

<sup>1</sup> Department of Materials and Production Technology Engineering, Faculty of Engineering, King Mongkut's University of Technology North Bangkok, Bangkok 10800, Thailand

<sup>2</sup> Biofunctional Materials and Devices Research Group, National Metal and Materials Technology Center, 114 Thailand Science Park, Phahonyothin Road, Khlong Nueng, Khlong Luang, Pathum Thani 12120, Thailand

<sup>3</sup> Center for Lightweight Materials, Design and Manufacturing, Department of Mechanical Engineering, Faculty of Engineering, King Mongkut's University of Technology Thonburi, 126 Pracha Uthit Road, Bang Mod, Thung Khru, Bangkok 10140, Thailand

Acrylonitrile-butadiene-styrene (ABS)-based composite filaments have been developed for strengthening purposes by adding reinforcement particles and fibers, for example, graphene oxide (GO), carbon fibers, zinc ferrite ( $\text{ZnFe}_2\text{O}_4$ ), and copper ferrite ( $\text{CuFe}_2\text{O}_4$ ) [10, 11]. Recently, mill scale (MS)-strengthened ABS composite filaments were presented as promising low-cost sustainable and high-strength raw materials. Iron oxide mill scale as solid waste from hot rolling milling was used to reinforce the ABS composite filaments [12], with tensile strength increasing by 45% when adding 1.0 vol% mill scale. Here, the effects of FFF 3D printing parameters on printability and mechanical properties were reported. Generally, mechanical properties of the printed PMC depend not only on composite filaments but also on printing parameters such as printing temperature, speed, and raster angle (the angle between nozzle paths and the plane of the printing platform) [13, 14]. Abeykoon et al. [15] investigated the effects of 3D printing parameters by optimizing process settings and improving polylactic acid (PLA) and ABS-printed structures and their properties. The highest modulus of PLA was 1538 MPa at infill density, printing temperature, and speed of 100%, 215 °C, and 90 mm s<sup>-1</sup>, respectively. The tensile modulus increased when increasing infill density and reducing porosity. In general, high infill densities provided enhanced mechanical properties and surface quality. By contrast, poor bonding between printing layers resulted from deficient melts at low temperatures, and high speed led to a decrease in the tensile modulus. Overflowing materials with low viscosity at high temperatures and low speeds reduced the cooling rate and changed the failure dimensions [16]. A linear infill pattern showed the highest tensile modulus because of strong layer bonding. Wang et al. [17] explored the mechanical properties of printed PEEK composites by varying the nozzle temperature between 400 and 440 °C and platform temperature between 240 and 280 °C. Increase in the former enhanced melting fluidity and formability, while increase in the latter improved infiltration and diffusion among the deposited filaments and interlayers, thereby reducing internal gaps and pore sizes. Increasing the nozzle temperature improved the raster bonding, leading to higher tensile properties [18]. Low printing speed of 5 mm s<sup>-1</sup> promoted printing stability, extrusion, and interlayer adhesion. Nevertheless, exceeding material printing limits of the nozzle temperature resulted in polymer degradation, leading to a decrease in surface quality and mechanical strength [19]. For instance, the study of Ouazzani et al. recently demonstrated that increasing the nozzle temperatures resulted in improved surface qualities of ABS by strengthening the bonding between adjacent filaments, while the over-printing temperature diminished the surface finish [20]. Another study by Badagu et al. also reported

that the surface roughness of 3D-printed ABS-ZrO<sub>2</sub> composite could be improved when printing at 240 °C with an infill percentage of 60% and a linear infill pattern [21].

Several previous studies [22–24] presented the optimal mechanical properties of PLA, ABS, and polyether-etherketone (PEEK) at the raster angle in parallel to tensile loads (0°). 3D-printed PLA specimens at this angle showed lower porosity than those built in other directions [25]. Zhang et al. [26] reported that printed PLA and Al/PLA composites at the raster angle paralleling the tensile direction showed good physical bonding and stress transfer between fibers and matrix, giving the highest tensile strength and dynamic mechanical properties. The samples were also broken through the individual raster layers. By contrast, the printed samples at the raster angle, perpendicular to the tensile direction (90°), showed the lowest tensile strength and failed under separations of the adjacent raster layers. This phenomenon was also observed using the Taguchi design of experiment method in the studies by Hasanzadeh et al. [27, 28]. The surface treatment is a significant process parameter that affects the mechanical properties of 3D-printed objects. Another investigation by Khosravani et al. disclosed that the tensile strength and fracture toughness of 3D-printed ABS parts decreased when subjected to surface treatment using a chemical solution like acetone [29]. The surface roughness was highest when the printing was done at a raster angle of 45°, due to the presence of tiled layers in the printed structures. Conversely, the lowest surface roughness was seen when the raster angle was set to 0° [30, 31].

For bonding failure, air gaps in the adjacent layers increased with decreasing infill density, causing high porosity in the printed structures [15]. Previous studies [15, 32, 33] observed the appearance of porosity in carbon fiber-reinforced polymer (CFRP) composite structures. Pore formation commonly occurs as a result of the incompatibility and poor bonding between the matrix and reinforcement, especially at high reinforcement percentages. However, the mechanical properties of CFRP still increased due to the predominant effect of the reinforcement. Furthermore, changing the infill percentage led to an obvious decrease in occurred porosities in the printed structures [34], hence enhancing the mechanical properties of the FFF printed samples [35, 36].

The mechanical behavior of PMC filaments and their printed parts was determined by finite element method (FEM)-based simulations [15, 37]. Ferretti et al. [38] modeled a representative volume element (RVE) with linear elastic property to predict local mechanical responses of PLA in two printing layers and 0.4 mm line width. The model demonstrated the macroscopic behavior of 3D-printed geometries with small deformation under an ideal assumption of good adhesion between layers. Wang et al. [25] developed a 2D RVE model with internal random pores characterized by X-ray computed tomography (XCT) analysis to predict

the macroscopic elastic properties of printed PLA materials. Sample simulation results with porosity lower than 7.9% correlated well with the corresponding experimental data.

To sum up, the fabrication of TPC filaments to strengthen metals and their oxide particulates has now created a new feedstock for FFF printing technology [11, 39, 40]. Recently, we have successfully developed novel ABS/MS composite filaments with improved mechanical properties and thermal conductivity via a simple melt-mixing method for the FFF 3D printing technique [12]. Prepared MS powder was added to ABS composite filament at up to 1.0 vol%. Enhanced mechanical properties of the composite filaments were attributed to the reinforcing mill scale fillers and compatibility with the ABS matrix. However, the influences of 3D printing parameters on the mechanical properties of FFF printed ABS/MS composites still require further investigation. This study is the first to investigate the physical and mechanical properties of printed ABS/MS composite objects prepared from mill scale (MS)-filled ABS composite filaments for the FFF 3D printing at different printing temperatures, speeds, and infill percentages. The motivation for the study is to develop printed ABS/MS composite filaments for high-strength 3D-printed ABS/MS composites by optimizing the process parameters of the FFF technique. The effects of printing parameters on air gap formation and surface finish of printed ABS/MS composite specimens were examined. FE-based RVE models of the printed composites were also generated as micromechanical modeling from real printed structures and irregular MS particle geometry, and local stress distributions in printing layers of the samples were also simultaneously assessed.

## 2 Experiment procedure

### 2.1 Materials

ABS pellets were obtained from IRPC Public Company Limited, Thailand, with melting temperature ( $T_m$ ), melt flow index (MFI), and shore hardness of 190–240 °C, 7 g/10 min (220 °C, 10 kg), and 85D, respectively. Mill scale with an average particle size of  $89.74 \pm 34.94 \mu\text{m}$  was prepared from recycling raw iron oxide mill scale powders (Sahaviriya Steel Industries PLC (Thailand)), according to the method described in our previous work [12]. The essential properties of MS have been analyzed and reported in the literature, i.e., phase composition by X-ray diffraction (XRD), particle morphology by scanning electron microscopy (SEM), and particle size distribution by a laser scattering particle size distribution analyzer LA-950 (Horiba) with PowderJet dry powder feeder system, transmittance (R) of 99.1%, and air at 0.3 MPa.

### 2.2 Fabrication of ABS/MS composite filament feedstock

3D printing acrylonitrile-butadiene-styrene (ABS) and MS composite filaments were prepared according to our previous study [12] (as shown in Fig. 1(a)). The ABS pellets were ground into a fine powder to obtain particle sizes of less than 1000  $\mu\text{m}$  using an ultra-centrifugal mill (ZM200) (Retsch GmbH, Germany). The ABS and MS powders were then dried overnight in a vacuum oven before mixing. Next, blends of ABS and MS were prepared with varied amounts of MS, i.e., 1.0 and 2.0 vol% (encoded as ABS/1.0%MS and ABS/2.0%MS, respectively) by manually shaking the mixture. Each ABS/MS compound was used for filament fabrication by the melt-blending method with a twin-screw extruder (Thermo Scientific Haake MiniLab II, Germany) at 235 °C to produce filaments with an average diameter of  $1.74 \pm 0.26 \text{ mm}$ .

### 2.3 3D printing of the ABS/MS composite filaments

After the filament fabrication, tensile and impact specimens were printed in a layer-by-layer fashion from each ABS/MS (ABS/1.0%MS and ABS/2.0%MS) composite filament using a fused filament fabrication (FFF) printer (Original Prusa i3 MK3S+, Prusa Research, Prague, Czech Republic) with a nozzle size of 0.8 mm (Fig. 1(b)). Tensile dog-bone-shaped specimens (19 mm width, 115 mm length, and 3 mm thickness) and impact specimens (12.70 mm width, 63.50 mm length, and 6.02 mm thickness) were prepared following the standard ASTM D638-10 (type IV) and ASTM D256-10 (Izod impact, Notched), respectively. SolidWorks software (SolidWorks 2020, Dassault Systèmes, SA, USA) and an open source (PrusaSlicer) were used to model and create files for printing. The FFF crucial printing parameters, e.g., printing temperatures, speeds, and infill densities, were studied because they directly affected the qualities and material properties of the as-printed objects [41]. To investigate the effects of printing parameters on the mechanical properties of 3D-printed ABS/MS composites, the varied printing temperatures, speeds, and infill densities of ABS/1.0%MS composites were studied as shown in Table 1. The ABS/2.0%MS composites were printed to compare with the former at one printing condition. For comparison, pure ABS specimens were also printed at 240 °C, 10 mm s<sup>-1</sup> speed, and 100% infill density. All printed samples were fabricated under the same printing parameters as follows: printing nozzle diameter of 0.8 mm, bed temperature of 100 °C, raster orientation of +45°/–45°, and flat build orientation.

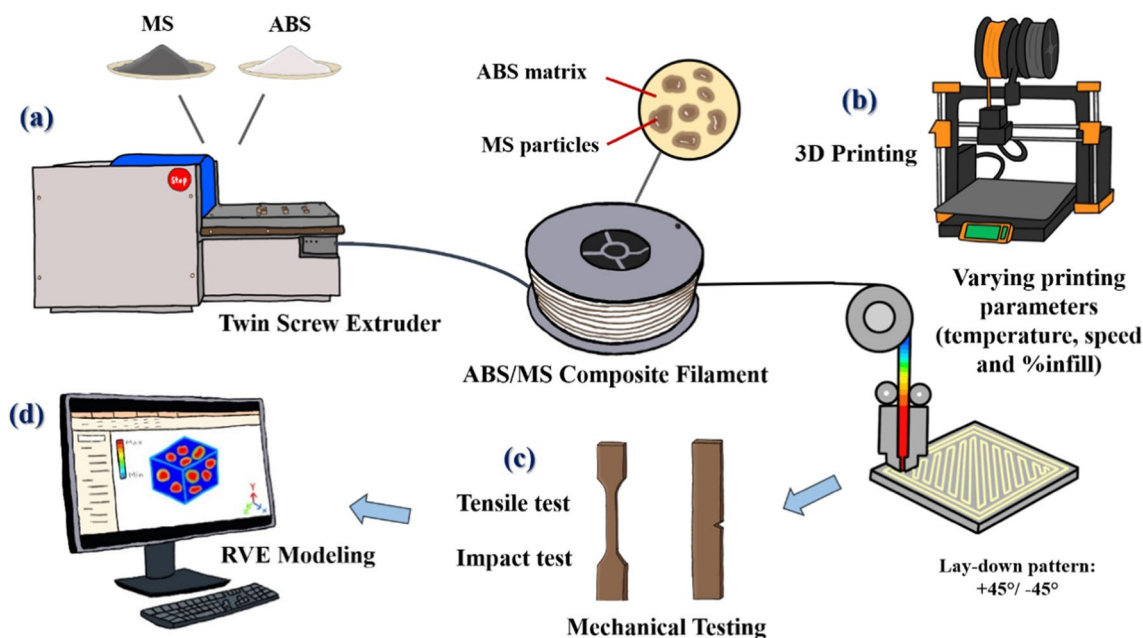


**Fig. 1** Schematic of the preparation of (a) ABS/MS composite filament, (b) 3D-printed specimen model viewed with lay-down pattern of +45°/−45° and flat build orientation, (c) Mechanical Testing and (d) Representative volume element (RVE) based modeling

**Table 1** Printing parameters for 3D-printed ABS/MS composites

Printing parameter	Variable value	
ABS/1.0%MS composite	Printing temperature (°C)	240–280 <sup>a</sup>
	Printing speed (mm s <sup>-1</sup> )	10–90 <sup>b</sup>
	Infill density (%)	25–100 <sup>c</sup>
ABS/2.0%MS composite	Printing temperature (°C)	270
	Printing speed (mm s <sup>-1</sup> )	10
	Infill density (%)	100

<sup>a</sup>At 10 mm s<sup>-1</sup> and 100 % infill

<sup>b</sup>At 270 °C and 100 % infill

<sup>c</sup>At 270 °C and 10 mm s<sup>-1</sup>

## 2.4 Morphological characteristics of ABS/MS composite filaments

The cross-sectional meso-structures of the printed ABS/MS composite samples after tensile tests were observed by an optical macro- and microscope (Olympus DXS1000, Japan). Mill scale particles and their arrangement in the composite specimens after printing were examined by  $\mu$ CT ( $\mu$ CT 35 SCANCO Medical Switzerland) with X-ray scanning at 60 kV, 250  $\mu$ A current at medium resolution setting (292  $\times$  1028 pixels with isotropic voxel size 10  $\mu$ m and integration time 438 ms). The  $\mu$ CT Evaluation Program V6.6 1680 was used to interpret the obtained  $\mu$ CT images. Finally, the surface finishes on the top of the printed ABS

composite specimens were observed by a 3D optical profiler (VR5000, KEYENCE, USA) with a wide-area 3D measurement mode as shown in Fig. 2(b).

## 2.5 Mechanical testing

### 2.5.1 Tensile test

Printed dog-bone specimens of pure ABS and ABS/MS composites were tested at room temperature, according to the standard ASTM D638-10, using a universal testing machine (Tinius Olsen H50KS, UK) equipped with a load cell of 50 kN and an extensometer (HT-8160) for the dimension of type IV specimen (25 mm gauge length) at crosshead speed of 10 mm min<sup>-1</sup>. At least three specimens were repeated for every printing condition.

### 2.5.2 Impact test

Notched Izod impact strength tests of the printed specimens were carried out using a pendulum impact tester (Zwick/Roell; HIT5.5P, Germany), according to the standard ASTM D256-10 with the 5.5 J pendulum at 25 °C. Three impact specimens were prepared for each printing condition with dimensions of 63.50 mm length, 12.70 mm width, and 6.02 mm height.

**Fig. 2** Digital photographs of (a) tensile test and (b) 3D surface measurement of 3D-printed ABS/MS composite specimens

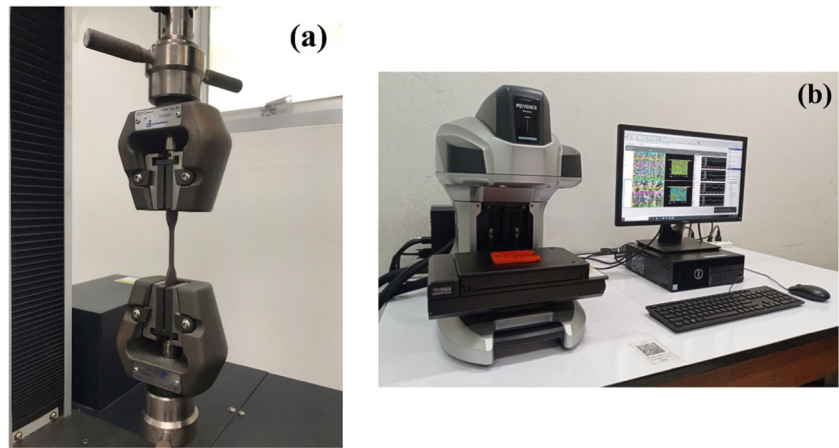


**Table 2** Factors and their levels of ANOVA

Factor	Level				
	1	2	3	4	5
Printing temperature (°C)	240	250	260	270	280
Printing speed (mm s <sup>-1</sup> )	10	30	50	70	90
Infill density (%)	25	50	75	90	100

## 2.6 Thermal conductivity testing

The thermal conductivity (TC) of the printed ABS/MS composites was measured by a thermal conductivity analyzer (Hot Disk AB: TPS2500S, Sweden) with a heating rate of 1.65 K min<sup>-1</sup> at 25 °C.

## 2.7 Analysis of variance

Analysis of variance (ANOVA) was applied to the experimental results from the mechanical tests to evaluate the significance of the studied printing parameters on determined mechanical properties with a 95% confidence level using IBM SPSS Statistics 28.0. The null hypothesis ( $H_0$ ) of no effect in the population was rejected if the  $p$ -value was less than 0.05. The factors and their levels are shown in Table 2.

## 3 Results and discussion

The ABS/1.0%MS composite filaments were successfully fabricated and printed as 3D specimens at the temperature of 270 °C, as reported in the previous study [12]. Adding 1.0 vol% mill scale significantly increased the tensile strength of the composite up to  $40.66 \pm 3.6$  MPa, higher than pure ABS at 45%. The homogeneous distribution of fine mill scale particles in the ABS composite matrix was illustrated, while several air gaps appeared along both edges of the printed specimens. The mechanical properties and morphological

characteristics of the printed ABS/1.0%MS composite using different printing parameters were also investigated.

### 3.1 Mechanical properties of the printed ABS/1.0%MS composites

The effects of various printing parameters on the mechanical properties, including tensile and impact strengths of the 3D-printed ABS/1.0%MS composite specimens, were investigated. A uniaxial tensile test was performed to determine key performances such as maximum stress, tensile modulus, and elongation at break, while specific absorption energy from the Izod impact test was the amount of energy absorbed per unit mass by a test specimen until breaking under impact load. The stress-strain curves of printed composite specimens are presented in the supporting information (Figure S1). As illustrated in Fig. 3, maximum stresses, tensile moduli, percent elongations at break, and specific energy absorptions of the printed ABS/1.0%MS composite specimens changed when the printing temperature increased within the range of 240 and 260 °C. At 270 °C, maximum stress, tensile modulus, and specific energy absorption significantly increased to  $40.13 \pm 1.32$  MPa,  $1644.33 \pm 70.05$  MPa, and  $14.91 \pm 1.08$  J m<sup>-1</sup> g<sup>-1</sup>, respectively, while elongation at break reduced. However, these parameters dramatically decreased at 280 °C, except for elongation at break that increased. Increasing printing temperatures led to enhanced tensile strength and stiffness of the FFF-printed specimens, ascribed to high temperatures promoting the flowability of the extruded material and good adhesion between the deposited layers of the 3D printed objects [16]. The over-heating temperature of 280 °C, compared to the melting temperature of pure ABS at 230–245 °C [16, 42], resulted in decreased stiffness and strength due to degradation of the ABS material under elevated temperatures, corresponding with a previous work of Behzadnasab and Yousefi [19].

The weights of the 3D-printed specimens and the designed objects from the CAD model were compared, as

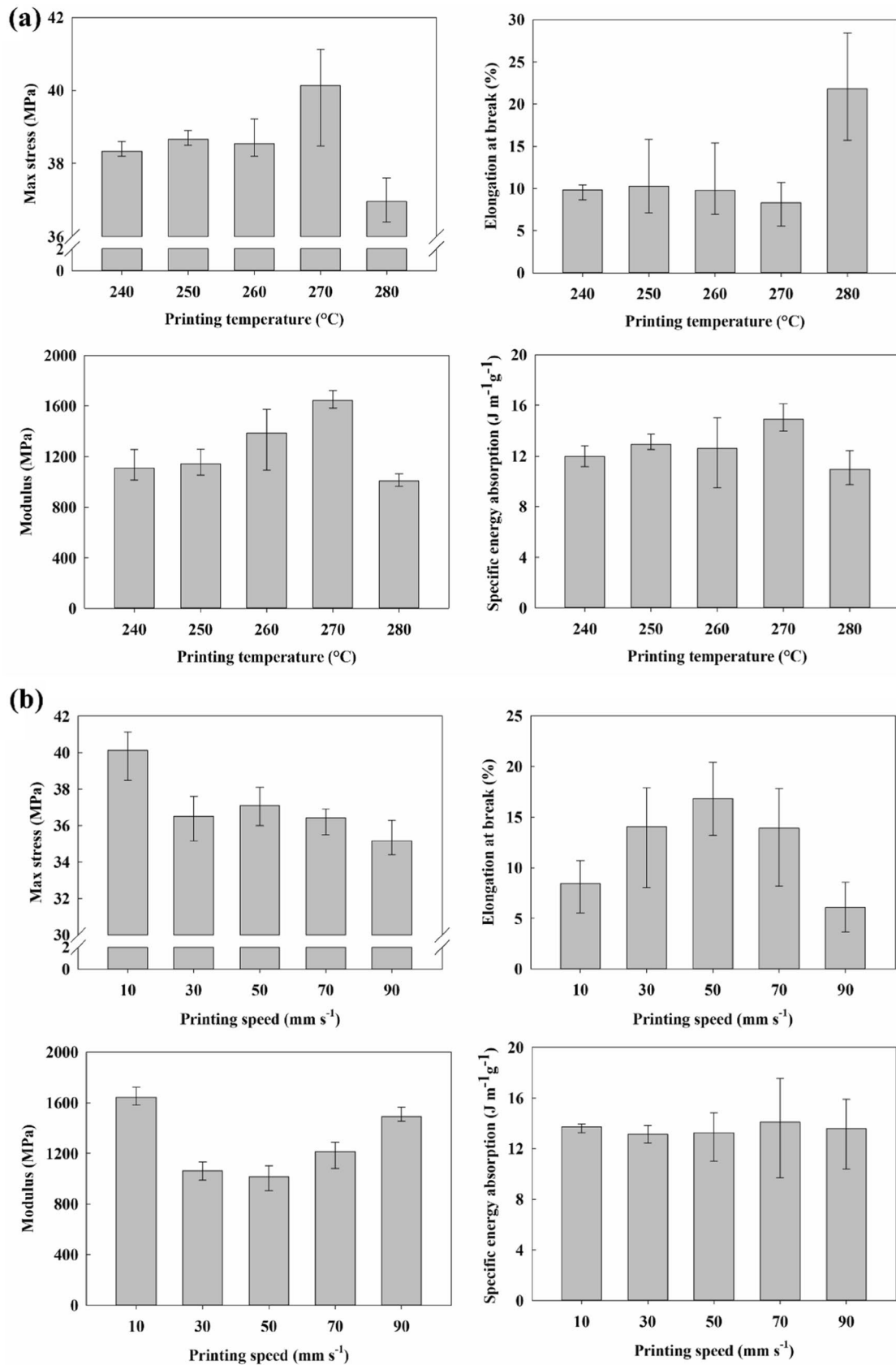


**Fig. 3** Maximum stresses, tensile moduli, elongations at break, and specific energy absorptions of printed ABS/MS composite specimens at different (a) printing temperatures, (b) printing speeds, and (c) infill densities

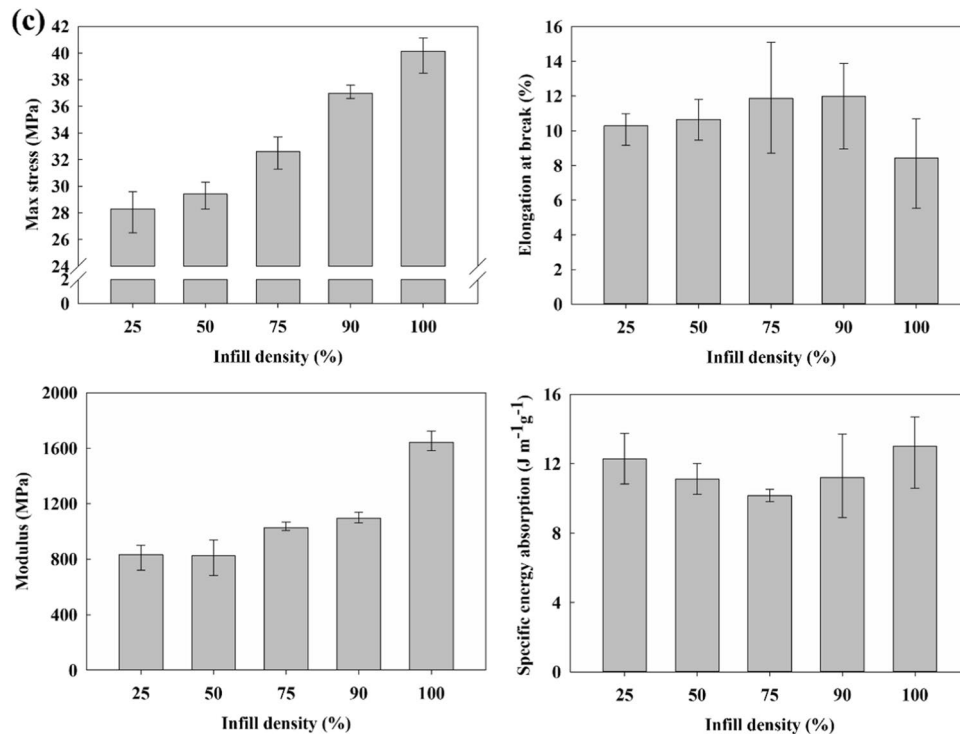
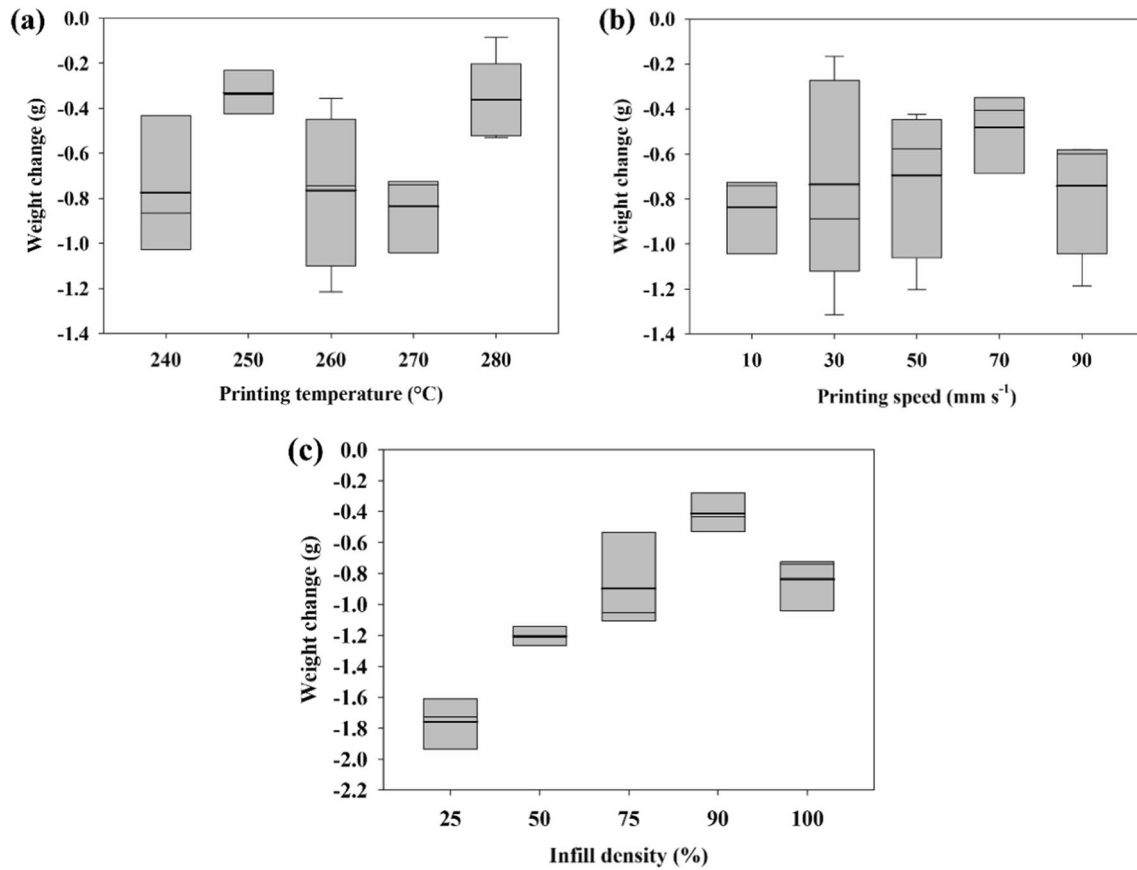


Fig. 3 (continued)

shown in Fig. 4. No significant effect of the printing temperature and printing speed on weight change was observed but infill density below 50% had a significant impact on the weight difference between the printed sample and the CAD model. Increasing the printing speed mainly influenced the elongation at break and tensile modulus of the printed composite specimens but their alterations had a reversal point. The analysis of variance (ANOVA) results in Table 3 showed maximum stresses and specific energy absorption energies at different printing speeds, presenting a regression  $p$ -value of more than 0.05 and indicating that the printing speed had no noticeable effect on these properties. By contrast, tensile modulus was greatest at a speed of  $10 \text{ mm s}^{-1}$  and sharply decreased by 35% when the printing speed increased to  $30 \text{ mm s}^{-1}$ . The values of the modulus remained constant at approximately  $1000 \text{ MPa}$  between the printing speeds of  $30$  and  $70 \text{ mm s}^{-1}$  and then increased to a higher value when the printing speed increased to  $90 \text{ mm s}^{-1}$ . Slow printing speed promoted a significant increase in the tensile modulus, associated with the strong filament-to-filament layer bonding and interlayer adhesion [16]. High values of elongation at break were achieved at printing speeds between  $50$  and  $70 \text{ mm s}^{-1}$ . The high infill density significantly enhanced the maximum stress and tensile modulus of the printed specimens with a  $p$ -value of 0.000. When adding more deposited materials, air gaps were reduced and the samples became denser and had higher weight, leading to improved mechanical

properties of the final printed parts. This observation agreed with Abeykoon et al. [15], who reported similar influences of processing conditions such as printing speed on properties of 3D-printed specimens (i.e., mechanical, thermal, and morphological). Results suggested that the most appropriate printing temperature, printing speed, and infill percentage of the printed ABS/MS composite in this study were  $270 \text{ }^\circ\text{C}$ ,  $10 \text{ mm s}^{-1}$ , and 100%, respectively, to achieve improved mechanical properties.

As previously mentioned, the optimal conditions for 3D printing of ABS/1.0%MS composite filaments were the printing temperature of  $270 \text{ }^\circ\text{C}$ , the printing speed of  $10 \text{ mm s}^{-1}$ , and the infill density of 100%. Figure 5 presents a comparison of the maximum stresses, elongations at break, tensile moduli, and specific energy absorptions of 3D-printed specimens fabricated from pure ABS and ABS/MS composite specimens containing 1.0 vol% and 2.0 vol% MS at the same optimal printing conditions. The first three properties of both the composite samples were similar while their tensile moduli and maximum stresses were higher than the pure ABS sample. By contrast, elongation of the composite samples reduced. The specific energy absorptions of the composites became more highly dependent on the volume fraction of mill scale and reached a maximum increase of 131% when 2.0 vol% mill scale was added. This increase in the specific energy absorption was in good agreement with Oksman et al., who reported an improvement of the



**Fig. 4** Weight changes between real 3D-printed specimens and their 3D CAD models

**Table 3** The ANOVA table showing maximum stress, percentage elongation at break, modulus, specific absorption energy, and weight change

Response	Source	DoF	Adj SS	Adj MS	F-value	p-value	Analysis
Maximum stress	Printing temperature	4	19.578	4.8944	9.50	0.001	Significant
	Printing speed	4	50.42	12.605	1.88	0.178	Insignificant
	Infill density	4	301.91	75.477	50.57	0.000	Significant
Percentage elongation at break	Printing temperature	4	538.4	134.61	7.24	0.003	Significant
	Printing speed	4	352.0	87.99	3.30	0.048	Significant
	Infill density	4	25.03	6.257	1.18	0.378	Insignificant
Modulus	Printing temperature	4	903873	225968	13.18	0.000	Significant
	Printing speed	4	1000599	250150	25.38	0.000	Significant
	Infill density	4	1345646	336411	48.74	0.000	Significant
Specific energy absorption	Printing temperature	4	22.84	5.710	1.00	0.437	Insignificant
	Printing speed	4	16.13	4.033	0.69	0.609	Insignificant
	Infill density	4	102.57	25.643	10.00	0.002	Significant
Weight change	Printing temperature	4	0.8632	0.21581	3.63	0.034	Insignificant
	Printing speed	4	0.2123	0.05309	0.46	0.762	Insignificant
	Infill density	4	2.8870	0.72174	14.57	0.000	Significant

DoF is degrees of freedom; Adj SS is the adjusted sum of squares; Adj MS is the adjusted mean square; Weight change is the weight difference between real 3D-printed specimens and a 3D object from a CAD model



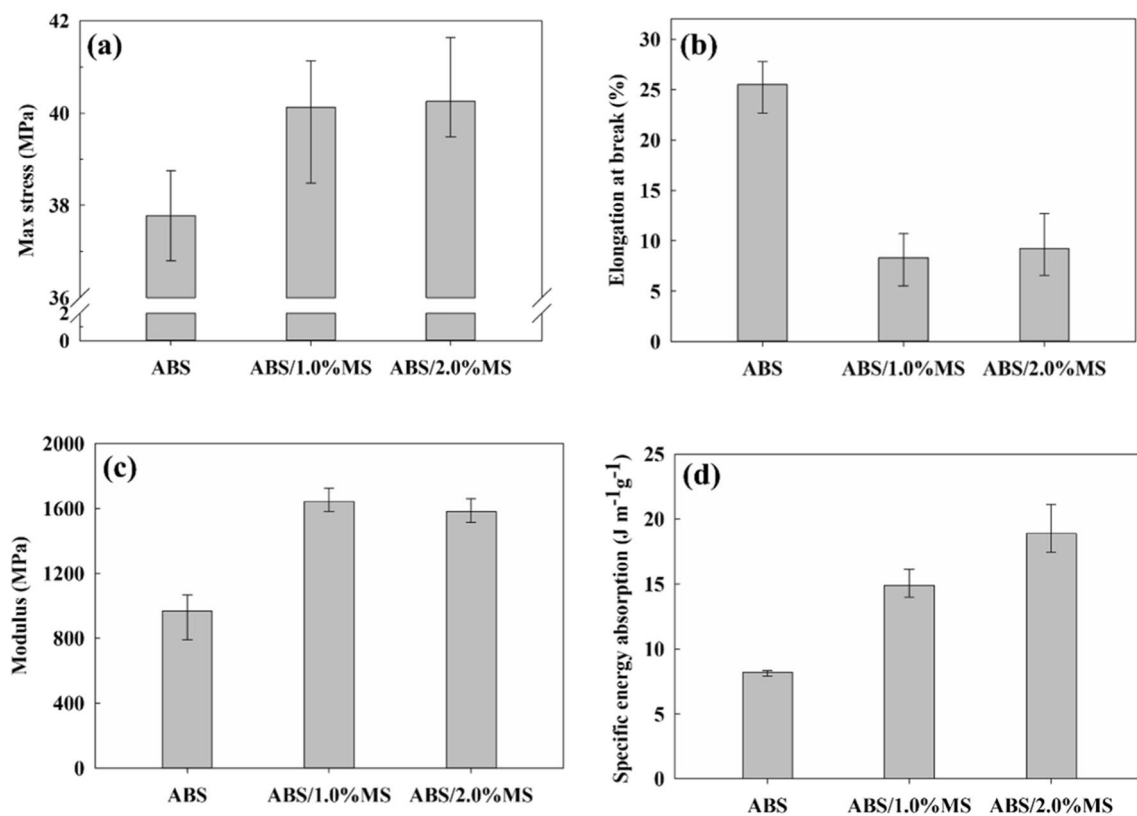


**Fig. 5** **a** Maximum stress, **b** elongation at break, **c** modulus, and **d** specific energy absorption of the printed ABS/1.0%MS and ABS/2.0%MS composite specimens

impact energy with higher amounts of natural fibers in PLA composites [43]. However, increasing MS content to 2.0 vol% did not significantly enhance the mechanical properties of the resulting filaments compared to the ABS/1.0%MS filaments, suggesting that the addition of at least 1.0 vol% of MS satisfactorily enhanced the mechanical properties of ABS/MS composite filaments. The investigation of higher MS percentages on the mechanical properties of the ABS/MS composites was limited in this study due to nozzle clogging problems during FFF printing.

### 3.2 Thermal properties of ABS composites

The thermal conductivity (TC) value of the ABS/1.0%MS composite specimen was determined as a function of temperature between 25 and 165 °C, and results were compared with pure ABS, as shown in Fig. 6. The TC values of the ABS/1.0%MS composite were higher than the pure ABS across all temperatures, attributed to the elevated TC of the iron oxide filler (5–15 W m<sup>-1</sup> K<sup>-1</sup> at room temperature) [38]. The TC values of both samples at room temperature agreed well with previous research [11, 39, 44]. At the initial temperature range, the TC values were constant but suddenly dropped at around 100 °C, close to

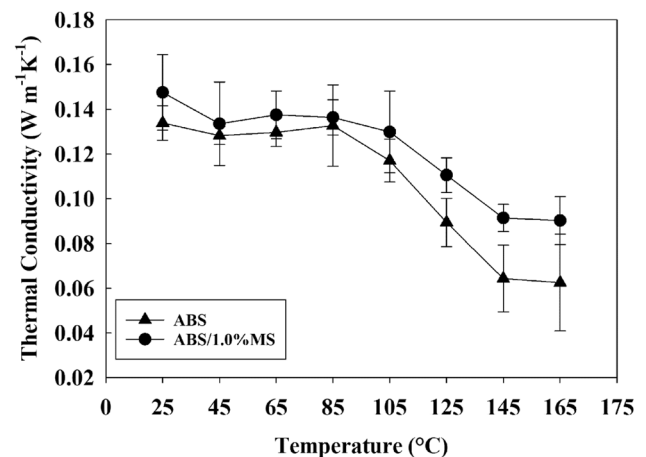


**Fig. 6** Thermal conductivity (TC) values of 3D-printed pure ABS and ABS/1.0%MS composite specimens as a function of temperature between 25 and 165 °C

the glass temperature ( $T_g$ ) of 108.84 and 109.08 °C for pure ABS and ABS/1.0%MS [12]. The decrease in thermal conductivity above  $T_g$  was caused by a decrease in the phonon velocity of ABS (amorphous polymers) [45].

### 3.3 Microstructural analysis and surface morphology of the printed composite

X-ray micro-computed tomography ( $\mu$ CT) was used to characterize particle dispersion in the 3D-printed ABS/1.0%MS composite by observing 3D-reconstructed images of cross-sectional printed composite dog-bones at the optimal printing condition. Dense mill scale particles were homogeneously distributed within the dog-bone-shaped head, body, and end regions of the specimen, as depicted in Fig. 7. However, the measured particle agglomeration and void distribution of these areas were different at  $15.18 \pm 0.11$  vol% and  $0.41 \pm 0.04$  vol% for the head,  $10.74 \pm 0.11$  vol% and  $2.91 \pm 0.04$  vol% for the body, and  $6.97 \pm 0.14$  vol% and  $0.15 \pm 0.03$  vol% for the end, respectively, as shown in Fig. 8. MS particle agglomeration was caused by the electrostatic

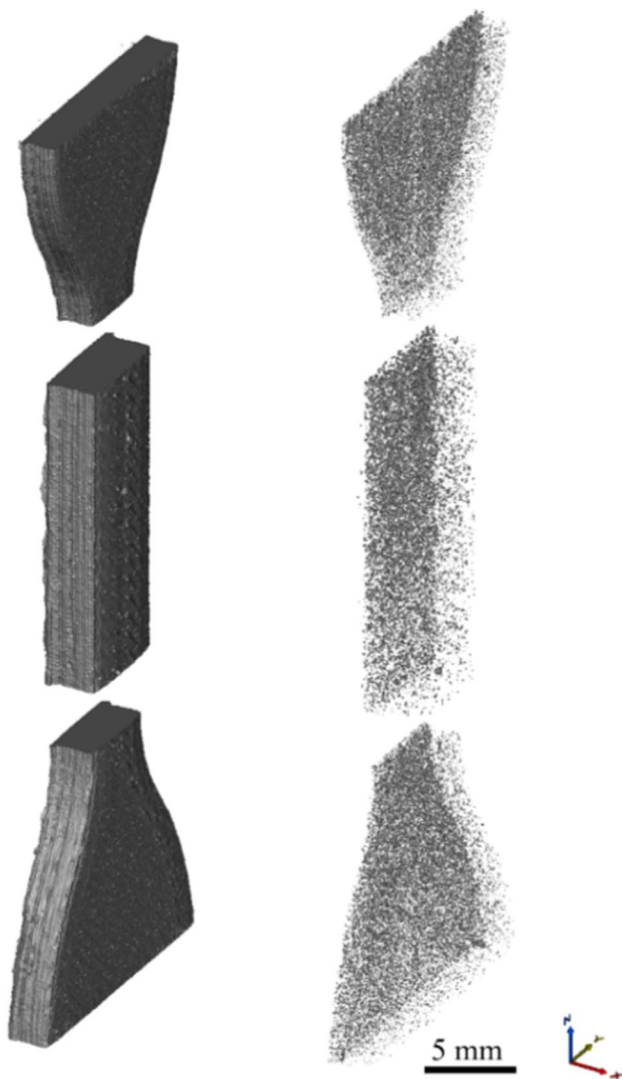


**Fig. 7**  $\mu$ CT micrographs of 3D-reconstructed images of the printed ABS/1.0%MS composite specimen

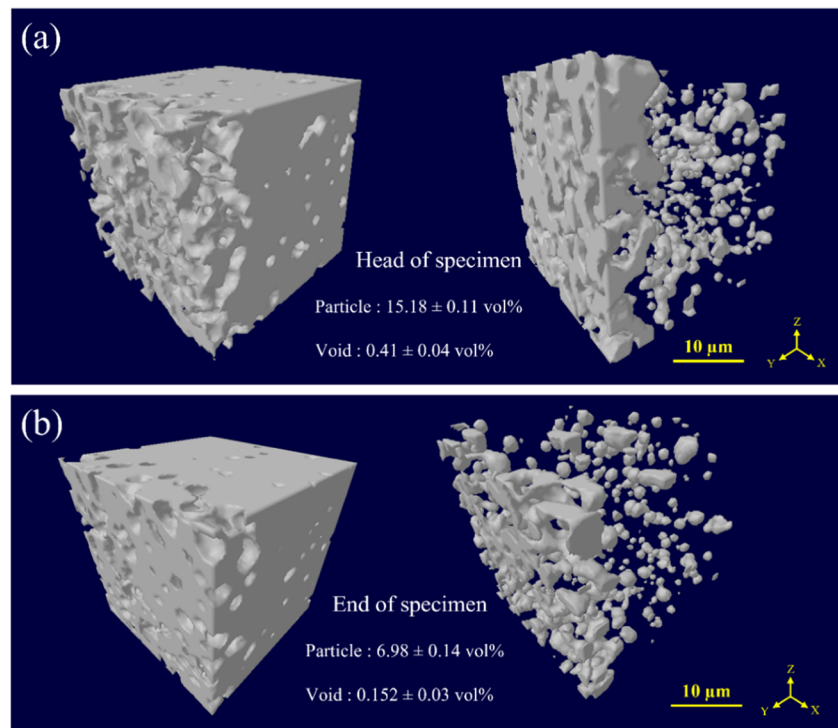
attraction of iron oxide particles [12] and the ferrimagnetic properties of magnetite ( $\text{Fe}_3\text{O}_4$ ) [46] in the iron oxide mill scale. The low percentages of particle clusters at the end were explained by the heat loss to the previously printed body and head parts while printing in the flat build orientation. This heat loss caused low printing temperature at the end, leading to low viscosity of molten material and limiting filler distribution and processability [16, 47].

The surface roughness of the printed specimens was measured by a 3D optical profiler with quantitative analysis, as illustrated in Fig. 8. A raster tool path inclined at  $45^\circ$  to the longitudinal axis was distinctly presented on the surface finish of the printed parts. The printed ABS/1.0%MS composite samples at high printing temperatures and speeds noticeably exhibited poor surface finish with high average roughness ( $R_a$ ) at 22.541 and 19.834, respectively, as shown in Fig. 9. These roughness values were higher than the appropriate printing condition at  $270^\circ\text{C}$  and  $10\text{ mm s}^{-1}$ . Several small pits (indicated by black arrows) occurred on the poor surface finish at  $280^\circ\text{C}$ , and some marks or flaws existed on the poor surface at  $90\text{ mm s}^{-1}$ . As discussed previously, the overflow of the composite material caused by slow cooling at high printing temperatures and lack of material at high printing speeds possibly led to dimension changes and poor final surfaces. As a consequence, the tensile modulus reduced. On the other hand, the surface quality significantly improved when the printing temperature and rate decreased.

### 3.4 Macro- and microstructural observations for the printed ABS composites

After the tensile tests, the macro- and microstructure of the fracture surfaces of the printed ABS/1.0%MS composite at failure were also investigated, as depicted in Figs. 10 and 11, respectively. For all printing conditions, typical brittle fractures were revealed on the printed composite samples. As shown in Fig. 12, the 3D images of the fracture surfaces at different printing temperatures revealed uneven surfaces between the printing layers, as well as gaps between two adjacent raster tool paths that corresponded to their fracture surfaces. The 3D images for the printed samples with varying speeds and infill densities are shown in the supporting information (Figure S2). Many air gaps representing spaces between two adjacent rasters [48] appeared on the entire composite structure printed at a low temperature of  $240^\circ\text{C}$ , especially at the edges. Their shapes resembled distorted triangles resulting from the used raster orientation of the crisscross ( $+45^\circ/-45^\circ$ ) [12, 16]. When printing at a higher temperature of  $270^\circ\text{C}$ , the air gaps in the center considerably decreased but remained at the edges. When printing at the temperature of  $280^\circ\text{C}$ , more homogeneous structures and regular rows of very small air gaps at  $54.89 \pm 24.39\ \mu\text{m}$  (measured by ImageJ software) at the edges

**Fig. 8**  $\mu$ CT micrographs of the cross-sectional printed ABS/1.0%MS composite specimen at (a) head and (b) end positions



were observed, with more compatibility of the mixtures of dark reinforcing mill scale particles and ABS matrix. The uniform microstructures increased the mechanical properties of the printed ABS composites at higher printing temperatures. The downsized triangular air gaps probably resulted from better agglomeration of the deposited filaments [47].

The highest porosity and air gaps occurred at the center of the composite structures printed at  $90 \text{ mm s}^{-1}$ . Poor bonding between deposited layers resulting from insufficient cooling time gave weakened deposited layers and larger air gaps of  $244.41 \pm 92.90 \mu\text{m}$ , corresponding to the lowest maximum stress at  $35.17 \pm 0.95 \text{ MPa}$  and elongation at break at  $6.05 \pm 2.45\%$  among all conditions as discussed previously and shown in Fig. 13. The air gaps dramatically increased five times when printing speeds increased from  $10$  to  $90 \text{ mm s}^{-1}$ , leading to a decrease of  $12.4\%$  in maximum stress. The ABS/1.0%MS composite specimen printed at an infill density of  $25\%$  showed sizable dark cavities at the center, giving the lowest maximum stress and tensile modulus. The pores diminished by three times when infill density increased by  $300\%$ , and the printed part became homogeneously dense with no air gaps at  $100\%$  infill density, contributing to an increased average maximum stress of  $40.13 \pm 1.65 \text{ MPa}$ .

#### 4 Finite element analysis of printed ABS/MS composites

The effect of air gaps on the mechanical properties of the printed ABS/1.0%MS composite was comprehensively studied using numerical FE modeling. FE simulation is a well-known numerical technique used as computational analysis tools for solving various problems of science and engineering with complicated geometry, loading, and materials properties. Hereby, FE-based RVE modeling was developed and microstructure-level simulations of the examined composite were conducted for determining local stress and strain distributions of critical areas of printed composite structures with and without air gaps. Such RVE model can reduce computational cost compared to other models of an entire test specimen. A real geometry of mill scale particles from the  $\mu$ CT scan technique was utilized to generate the reinforcing MS particles at  $1.0 \text{ vol}\%$  in the RVE model. The defined material data of the reinforcement and matrix are shown in Table 4, in which the properties of hematite were considered for the examined mill scales. 3D microstructure-based RVE models with dimensions of  $0.6 \text{ mm width} \times 0.6 \text{ mm}$

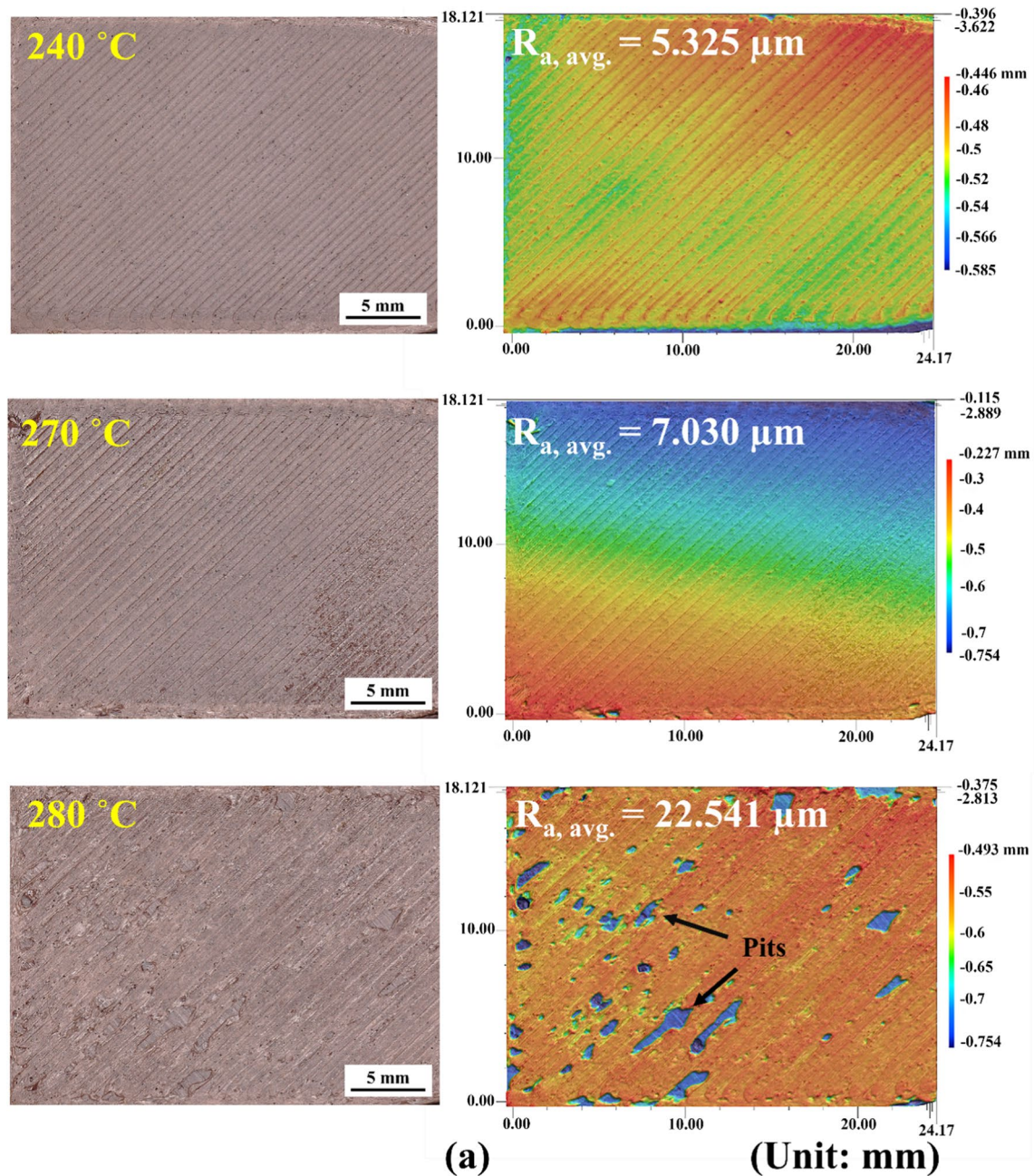


**Fig. 9** Scanned surface roughness of the printed composite specimens at different (a) printing temperatures and (b) printing speeds. Black arrows indicate small pits

length  $\times$  0.6 mm thickness were constructed according to the microstructures of the printed composite obtained from the optimal printing parameters for the center and edge regions. An RVE model with air gaps was created for the case of the edge area, while another model without air gaps described the composite material at the center area. Triangular elements were used for discretizing the model, with the total number of elements at 112,000 for both cases, as shown in Fig. 14. From the simulations, Figs. 15 and 16 show high

von Mises stresses occurring around the mill scale particles compared to other regions of the matrix in both RVE models with and without air gaps, respectively. By contrast, the equivalent plastic strains of the mill scale particles were low and negligible because of their higher hardness value. High stress concentrations appeared at the sharp corners of irregular particles. Our results agreed with previous studies [50, 51], in which angular and irregular reinforced particles caused higher stress concentrations than other particles

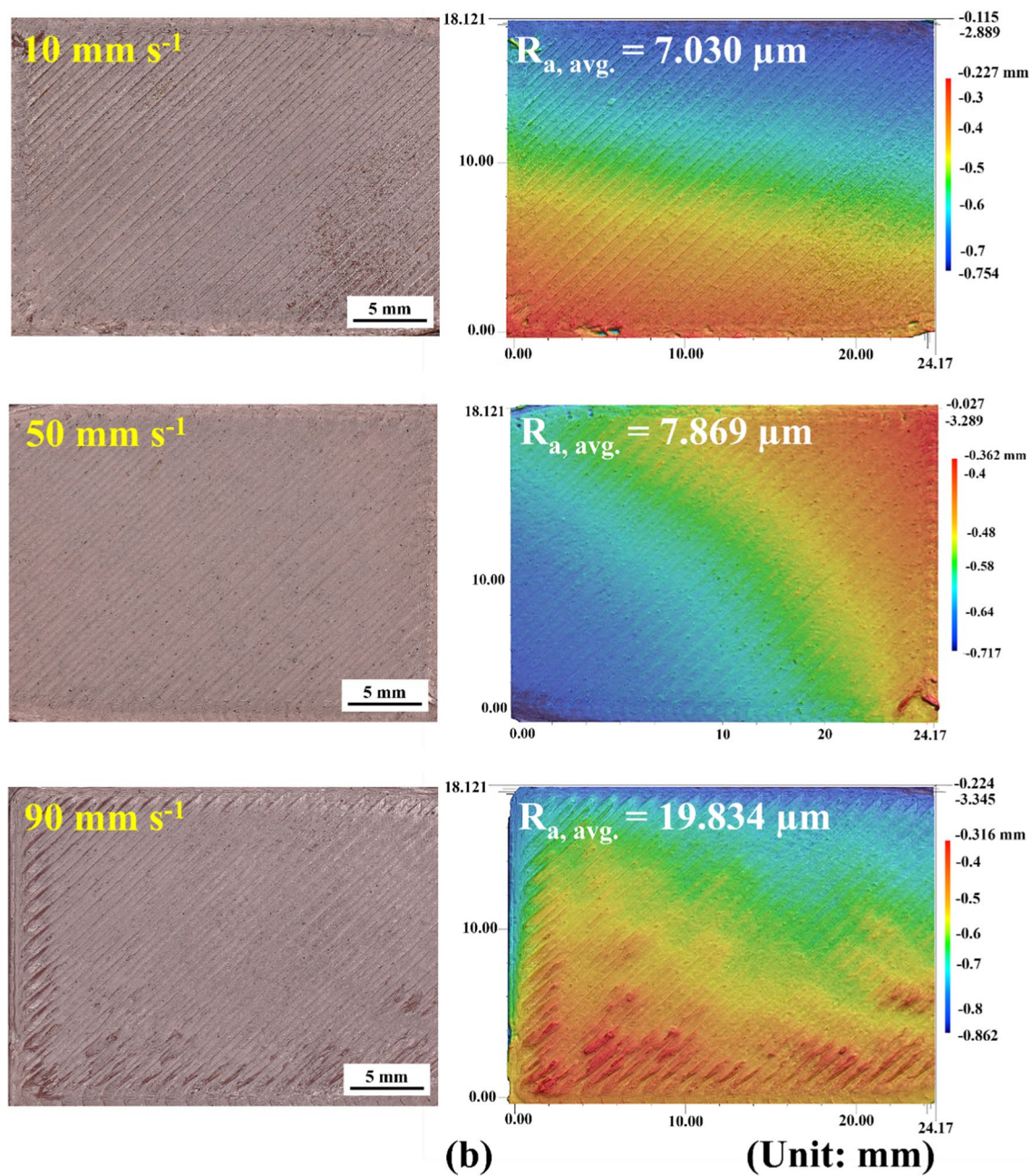
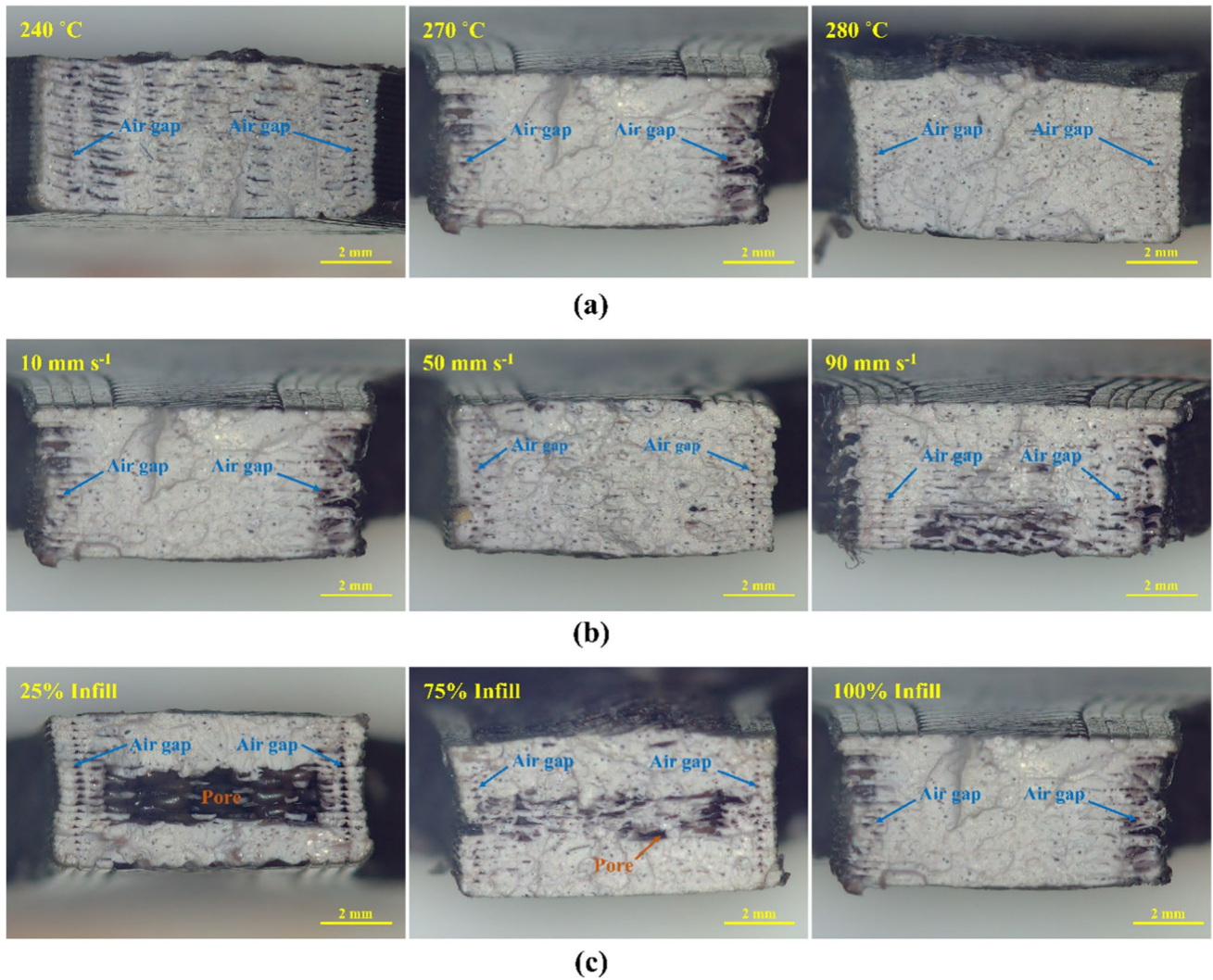


Fig. 9 (continued)

with spherical and ellipsoidal shapes, thereby offering more uniform load transfer between particle and matrix. When comparing the results from mill scale particles with different sizes and sphericities ( $S_p$ ) computed from Eq. 1, the largest particle (no. 3) at  $0.605 \mu\text{m}$  and  $S_p$  of 0.93 exhibited higher maximum stress at  $55.79 \pm 0.55 \text{ MPa}$  than particles no. 2 ( $52.15 \pm 1.02 \text{ MPa}$ ) and no. 1 ( $51.90 \pm 6.46 \text{ MPa}$ ), respectively. Particle size played a vital role in high stress development around the reinforcement particles. Likewise, high stress concentration was revealed near the corners of

triangular air gaps, leading to crack initiation and propagation. Furthermore, the stress–strain curves of the 3D RVE model were similar to the experimental results, as shown in Fig. 17. The predicted curves of the model with air gaps were lower than for the model without air gaps because of mass reduction. Therefore, the RVE model can be further developed to predict the mechanical properties of ABS composites at various printing conditions for different volume fractions of MS and air gaps.



**Fig. 10** Optical images of macrostructures of fracture surfaces of printed ABS/1.0%MS composite samples after tensile tests at different (a) printing temperatures, (b) printing speeds, and (c) infill densities

$$S_p = \frac{\pi^{1/3} (6V_p)^{2/3}}{A_p} \quad (1)$$

where  $V_p$  = volume of particles and  $A_p$  = surface area of particles.

## 5 Conclusions

The present study investigated the physical and mechanical properties of the 3D-printed ABS/MS composites at different printing temperatures, speeds, and infill percentages to optimize the process parameters for achieving high mechanical properties and surface qualities. The most essential findings of this work can be drawn as follows.

- The printability of MS-strengthened ABS composites was investigated at different printing temperatures, speeds, and infill densities, with results confirming the product as a candidate for low-cost sustainable raw material for FFF technology. High printing temperature promoted an appropriate melt for good bonding between printing layers and produced a more homogenous structure with tiny air gaps, thereby increasing the tensile properties and impact energy of the ABS/1.0%MS composite. Similarly, a slow printing speed gave sufficient cooling time for deposition and bonding, and the high infill density provided a denser printing structure.
- An increase in air gap size appeared at high printing speeds and low infill density. The air gaps were enlarged five times when printing speed increased from 10 to 90 mm s<sup>-1</sup> and three times when reducing infill density from 100 to 25%.

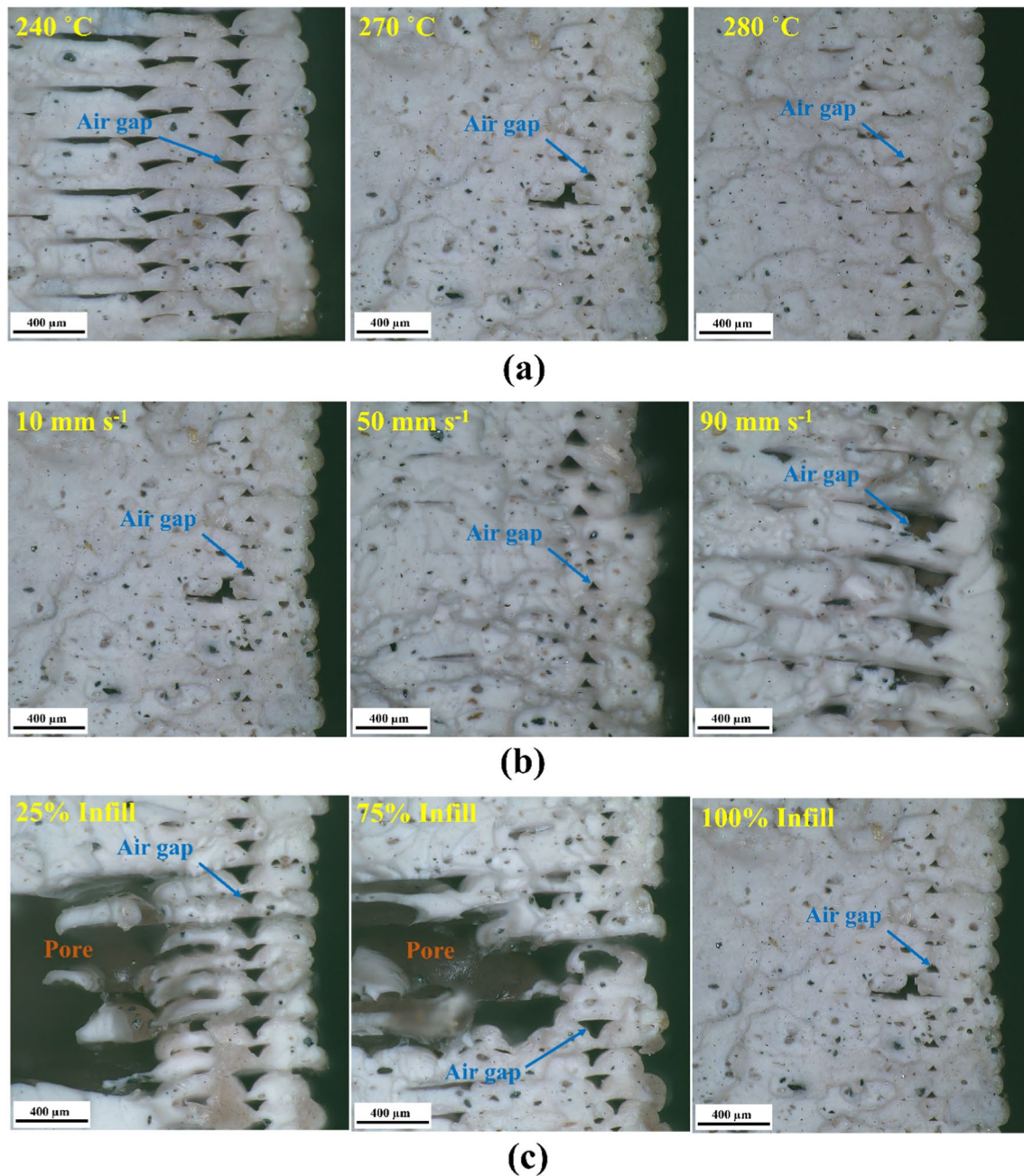


**Fig. 11** Optical macrostructural images at high magnification of the fracture surfaces of printed ABS/1.0%MS composite samples (at right edges) after tensile tests at different (a) printing temperatures, (b) printing speeds, and (c) infill densities

- Optimal printing conditions of the ABS/1.0%MS composite were 270 °C, 10 mm s<sup>-1</sup>, and 100% infill. Beyond this optimal printing temperature and speed, tensile strength and impact energy decreased, and the final surface of the ABS composite samples was poor. The homogenous dense distribution of mill scale particles, shown by X-ray micro-computed tomography, verified the printability at the optimal condition. Particle agglomeration occurred during printing, possibly due to the electrostatic attraction behavior and the ferrimagnetic properties of iron oxide particles in the ABS matrix.
- Reinforcing mill scale particles with high TC of iron oxide significantly enhanced the thermal conductivity value of the ABS/1.0%MS composite by 1.2–1.7 times higher than pure ABS at temperatures between 25 and 165 °C.
- Maximum stresses, elongations at break, and tensile moduli of the printed ABS composites at 1.0 vol% and

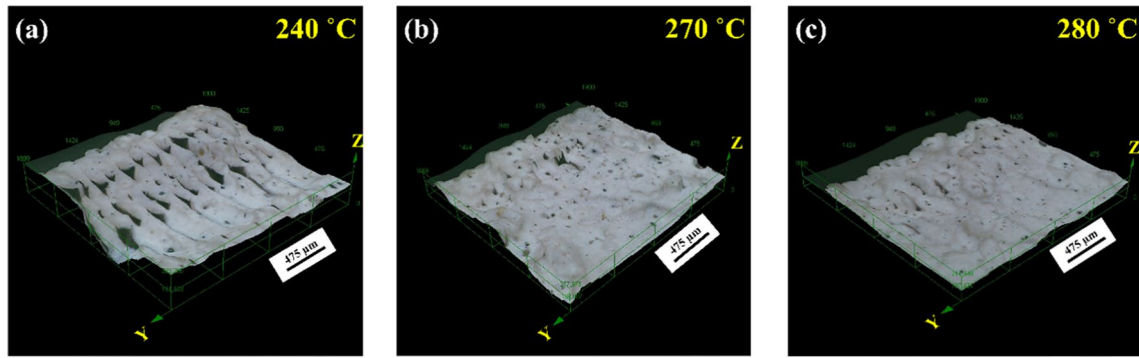


**Fig. 12** 3D images of fracture surfaces of tensile ABS/1.0%MS composite samples at different printing temperatures (10 mm s<sup>-1</sup> and 100% infill)

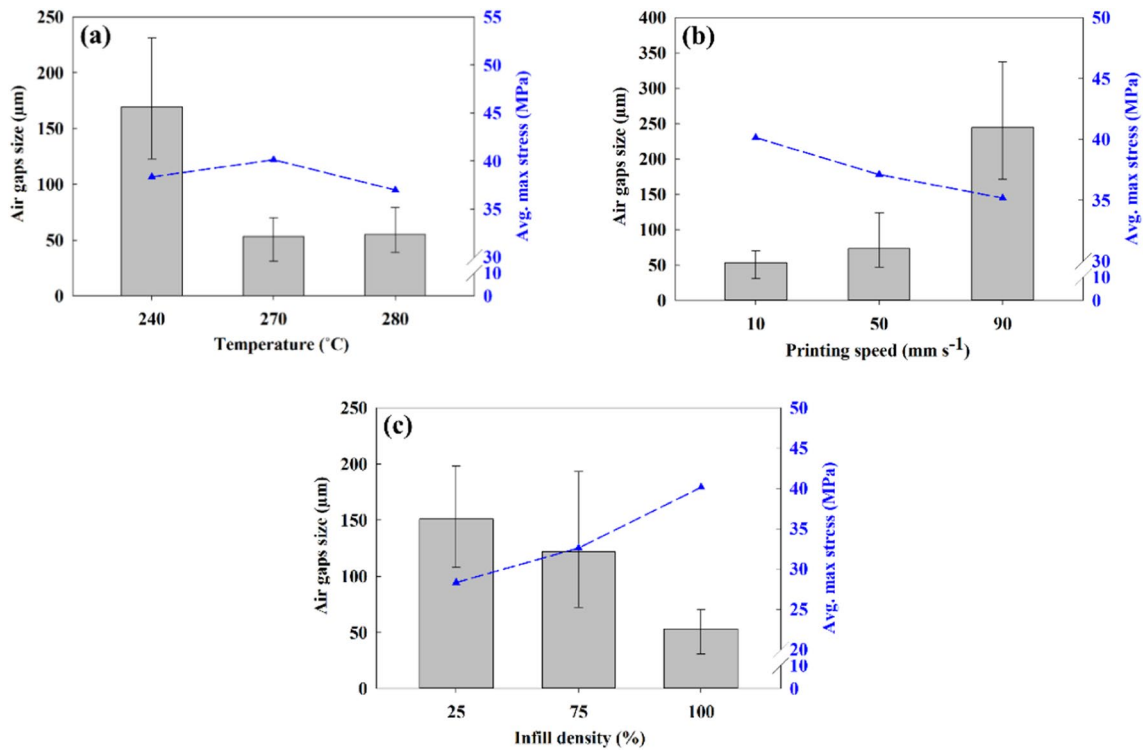


**Fig. 13** Comparisons between air gap size and average maximum stress of printed composite specimens at different (a) printing temperatures, (b) printing speeds, and (c) infill densities

**Table 4** Material properties of the constituents in the RVE model

Material properties		
Physical property	ABS	Hematite [49]
Mass density (t mm <sup>-3</sup> )	1.01×10 <sup>-9</sup>	5.25×10 <sup>-9</sup>
Young's modulus (MPa)	1193.1	359,000
Poisson's ratio (-)	0.35	0.12

2.0 vol% were similar. However, the specific energy absorptions of the latter were higher by 1.3 times.

- The predicted stress and strain distributions by the RVE model exhibited high stress concentrations at the pole of real angular mill scale particles and at the sharp corners of the triangular air gaps.

In summary, the developed 3D printable ABS/MS composite materials for FFF technique and the systematic study of printing parameters including FE-based simulations in this work introduced a new class of composite



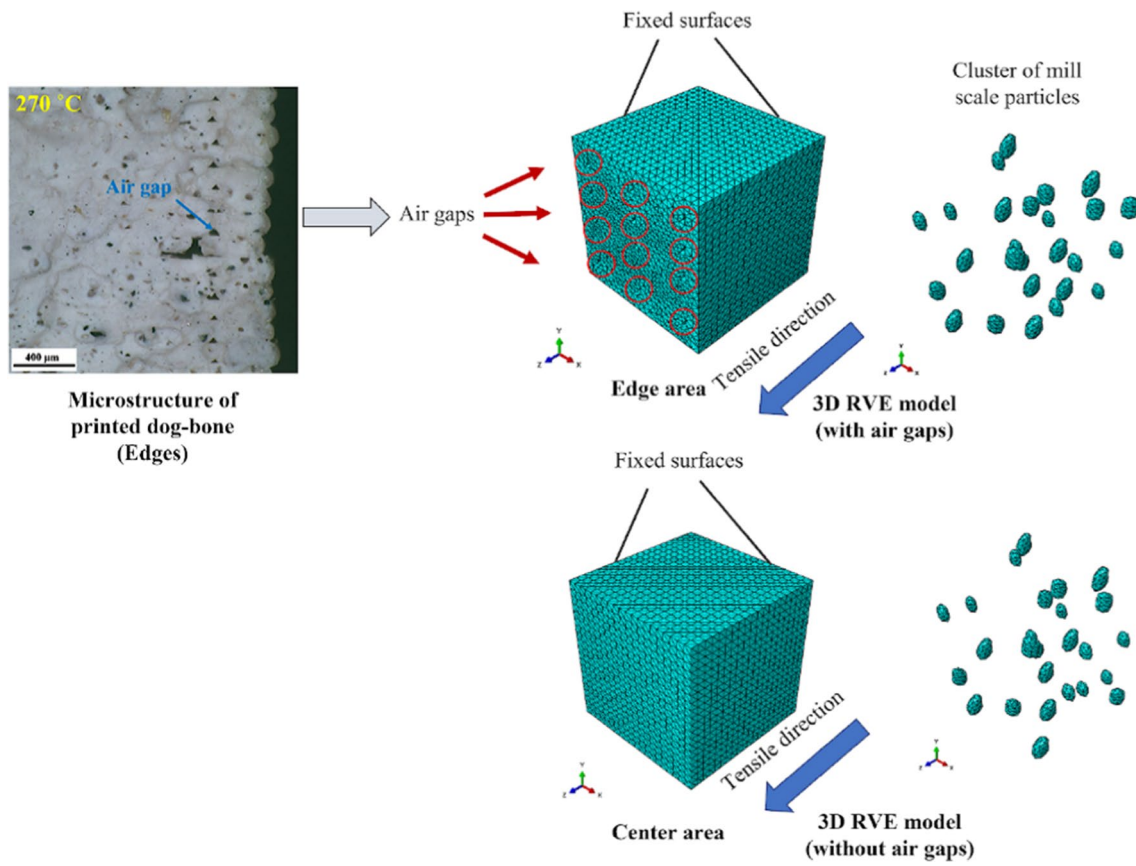


Fig. 14 3D microstructure-based models of printed composite structures with and without air gaps

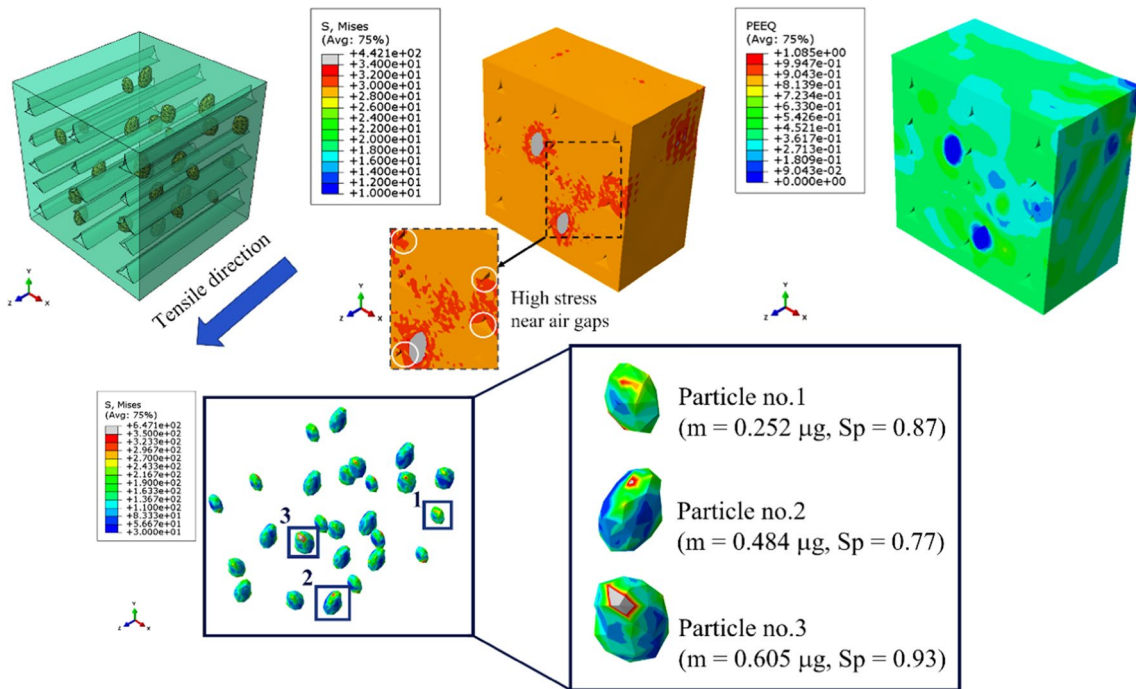
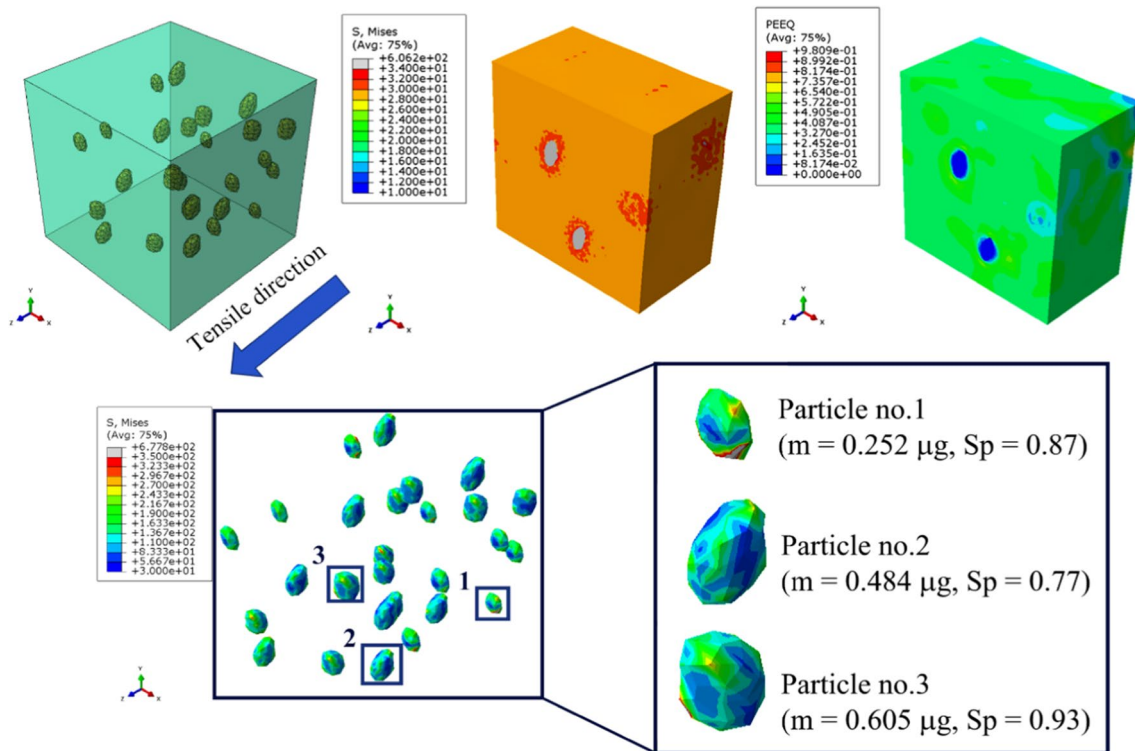
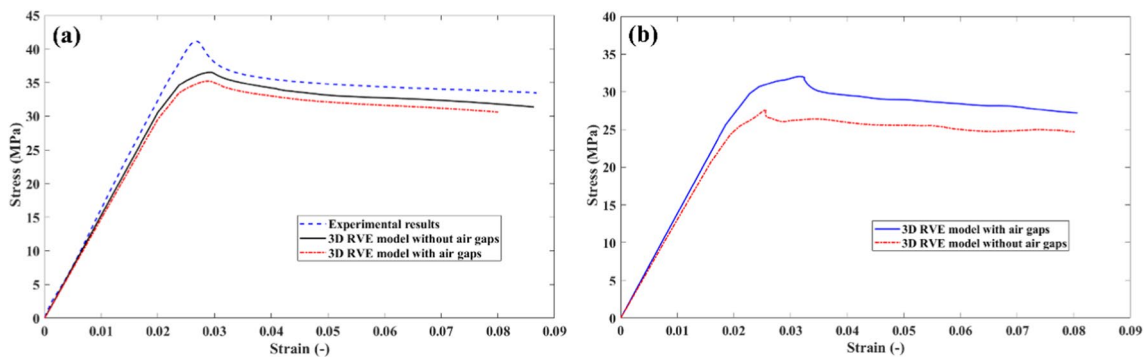


Fig. 15 Predicted equivalent stress and strain distributions of the RVE model with air gaps



**Fig. 16** Predicted equivalent stress and strain distributions of the RVE model without air gaps



**Fig. 17** Stress–strain curves of (a) 3D RVE models compared to experimental results and (b) 3D RVE models with surrounding particles

materials with more specific and functional properties, which exhibited potential uses in engineering applications such as reinforced polymer and high strength structural parts. However, addition of the MS in the ABS matrix obviously showed a content limitation, partly owing to its poor dispersion in the polymeric matrix during the filament-making process and nozzle clogging during a FFF printing. Hence, interplays between the MS powder contents (greater than 1.0 vol%), filament preparation, and FFF printing parameters have significant effects on the qualities of 3D-printed parts and should be further investigated in more details for achieving 3D-printed objects

possessing both satisfactory dimensional stability and increased mechanical properties.

**Acknowledgements** This research study was supported by King Mongkut's University of Technology North Bangkok under contract no. KMUTNB-67-KNOW-05. The authors acknowledge the National Metal and Materials Technology Center (MTEC), Thailand, for providing facilities through the Biofunctional Materials and Devices Research Unit. We would like to thank Mr. Phachai Kungwankrai and Mr. Suksan Muengto for technical assistance in filament extrusion and 3D printing.

**Author contribution** Jennarong Tungtrongpaioj: conceptualization, experimental design, methodology, software, data curation, writing—original draft, visualization, investigation, software, validation,

funding acquisition. Korbkaroon Doungkeaw: methodology, carrying out measurements and calculation. Boonlom Thavornnyutikarn: experimental design, methodology, writing—review and editing. Peeraphat Suttipong: software, simulation. Vitoon Uthaisangsuk: writing—review and editing, investigation, supervision.

**Data availability** The raw/processed data required to reproduce these findings cannot be shared as the data also forms part of an ongoing study.

## Declarations

**Competing interests** The authors declare no competing interests.

## References

- Buchanan C, Gardner L (2019) Metal 3D printing in construction: a review of methods, research, applications, opportunities and challenges. *Eng Struct* 180:332–348. <https://doi.org/10.1016/j.engstruct.2018.11.045>
- Sama SR, Badamo T, Lynch P et al (2019) Novel sprue designs in metal casting via 3D sand-printing. *Addit Manuf* 25:563–578. <https://doi.org/10.1016/j.addma.2018.12.009>
- Thompson MK, Moroni G, Vaneker T et al (2016) Design for additive manufacturing: trends, opportunities, considerations, and constraints. *CIRP Annals* 65:737–760. <https://doi.org/10.1016/j.cirp.2016.05.004>
- Grand View Research (2021) Additive manufacturing market size, share & trends analysis report by component, by printer type, by technology, by software, by application, by vertical, by material, by region, and segment forecasts, 2022–2030. <https://www.grandviewresearch.com/industry-analysis/additive-manufacturing-market#>. Accessed 17 Oct 2023
- Chartier T, Badev A (2013) Rapid prototyping of ceramics. In: *Handbook of Advanced Ceramics: Materials, Applications, Processing, and Properties*, 2nd edn, pp 489–524
- Kumar R, Singh R, Ahuja I (2019) Joining of 3D printed dissimilar thermoplastics with consumable tool through friction stir spot welding: a case study. In: *Encyclopedia of Renewable and Sustainable Materials*, pp 1–5. <https://doi.org/10.1016/B978-0-12-803581-8.11529-2>
- Mohamed O, Masood S, Bhowmik J (2022) Experimental and statistical modeling on surface roughness for FDM PC-ABS polymeric material using D-optimal design. In: *Reference Module in Materials Science and Materials Engineering*. <https://doi.org/10.1016/B978-0-12-820352-1.00103-6>
- Tian X, Todoroki A, Liu T et al (2022) 3D printing of continuous fiber reinforced polymer composites: development, application, and prospective. *Chinese Journal of Mechanical Engineering: Additive Manufacturing Frontiers* 1:100016. <https://doi.org/10.1016/j.cjmeam.2022.100016>
- Zhang H, Wu Y, Wang K et al (2020) Materials selection of 3D-printed continuous carbon fiber reinforced composites considering multiple criteria. *Mater Des* 196:109140. <https://doi.org/10.1016/j.mates.2020.109140>
- Aumnate C, Pongwisuthiruchte A, Pattananuwat P et al (2018) Fabrication of ABS/graphene oxide composite filament for fused filament fabrication (FFF) 3D printing. *Adv Mater Sci Eng* 2018:1–9. <https://doi.org/10.1155/2018/2830437>
- Aqzina SS, Yeoh CK, Idris MS et al (2018) Effect of different filler content of ABS-zinc ferrite composites on mechanical, electrical and thermal conductivity by using 3D printing. *J Vinyl Addit Technol* 24:E217–E229. <https://doi.org/10.1002/vnl.21640>
- Tungtrongpaioj J, Doungkeaw K, Thavornnyutikarn B et al (2023) Mill scale strengthened ABS composite filaments for 3D printing technology. *J Mater Sci* 58:4165–4183. <https://doi.org/10.1007/s10853-023-08274-0>
- Wu W, Ye W, Wu Z et al (2017) Influence of layer thickness, raster angle, deformation temperature and recovery temperature on the shape-memory effect of 3D-printed polylactic acid samples. *Materials* (Basel) 10. <https://doi.org/10.3390/ma10080970>
- Niendorf K, Raeymaekers B (2021) Additive manufacturing of polymer matrix composite materials with aligned or organized filler material: a review. *Adv Eng Mater* 23:2001002. <https://doi.org/10.1002/adem.202001002>
- Abeykoon C, Sri-Amphorn P, Fernando A (2020) Optimization of fused deposition modeling parameters for improved PLA and ABS 3D printed structures. *Int J Lightweight Mater Manuf* 3:284–297. <https://doi.org/10.1016/j.ijlmm.2020.03.003>
- Dave HK, Davim JP (eds) (2021) *Fused deposition modeling based 3D printing*. Materials forming, machining and tribology. Springer, Cham, Switzerland
- Wang P, Zou B, Ding S et al (2021) Effects of FDM-3D printing parameters on mechanical properties and microstructure of CF/PEEK and GF/PEEK. *Chin J Aeronaut* 34:236–246. <https://doi.org/10.1016/j.cja.2020.05.040>
- Mihankhah P, Azdast T, Mohammadzadeh H et al (2023) Fused filament fabrication of biodegradable polylactic acid reinforced by nanoclay as a potential biomedical material. *J Thermoplast Compos Mater* 36:961–983. <https://doi.org/10.1177/08927057211044185>
- Behzadnasab M, Yousefi A (2016) Effects of 3D printer nozzle head temperature on the physical and mechanical properties of PLA based product. 12th International Seminar on Polymer Science and Technology. Islamic Azad University. Tehran, Iran
- Ouazzani K, El Jai M, Akhrif I et al (2023) An experimental study of FDM parameter effects on ABS surface quality: roughness analysis. *Int J Adv Manuf Technol* 127:151–178. <https://doi.org/10.1007/s00170-023-11435-9>
- Badogu K, Kumar R, Kumar R (2023) Investigations on hardness and surface roughness of 3D printed ABS-ZrO<sub>2</sub> composite structures for post processing applications. *Materials Today: Proceedings*. <https://doi.org/10.1016/j.matpr.2023.11.032>
- Zheng J, Dong E, Kang J et al (2021) Effects of raster angle and material components on mechanical properties of polyether-etherketone/calcium silicate scaffolds. *Polymers* (Basel) 13. <https://doi.org/10.3390/polym13152547>
- Srinivasan Ganesh Iyer S, Keles O (2022) Effect of raster angle on mechanical properties of 3D printed short carbon fiber reinforced acrylonitrile butadiene styrene. *Compos Commun* 32:101163. <https://doi.org/10.1016/j.coco.2022.101163>
- Algarni M (2021) The influence of raster angle and moisture content on the mechanical properties of PLA parts produced by fused deposition modeling. *Polymers* (Basel) 13. <https://doi.org/10.3390/polym13020237>
- Wang X, Zhao L, Fuh JYH et al (2019) Effect of porosity on mechanical properties of 3D printed polymers: experiments and micromechanical modeling based on X-ray computed tomography analysis. *Polymers* (Basel) 11. <https://doi.org/10.3390/polym11071154>
- Zhang X, Chen L, Mulholland T et al (2019) Effects of raster angle on the mechanical properties of PLA and Al/PLA composite part produced by fused deposition modeling. *Polym Adv Technol* 30:2122–2135. <https://doi.org/10.1002/pat.4645>
- Hasanzadeh R, Mihankhah P, Azdast T et al (2023) Optimization of process parameters of fused filament fabrication of polylactic acid composites reinforced by aluminum using Taguchi approach. *Metals* 13:1013. <https://doi.org/10.3390/met13061013>

28. Hasanzadeh R, Mihankhah P, Azdast T et al (2023) Biocompatible tissue-engineered scaffold polymers for 3D printing and its application for 4D printing. *Chem Eng J* 476:146616. <https://doi.org/10.1016/j.ccej.2023.146616>
29. Khosravani MR, Anders D, Reinicke T (2023) Effects of post-processing on the fracture behavior of surface-treated 3D-printed parts. *CIRP J Manuf Sci Technol* 46:148–156. <https://doi.org/10.1016/j.cirpj.2023.08.006>
30. Hanon M, Zsidai L (2023) Investigation on the accuracy, hardness, and surface roughness of photopolymerization 3D printing technique objects. *AIP Conf Proc* 2607:120003-1–120003-5. <https://doi.org/10.1063/5.0135763>
31. Çakan BG (2021) Effects of raster angle on tensile and surface roughness properties of various FDM filaments. *J Mech Sci Technol* 35:3347–3353. <https://doi.org/10.1007/s12206-021-0708-8>
32. Ning F, Cong W, Qiu J et al (2015) Additive manufacturing of carbon fiber reinforced thermoplastic composites using fused deposition modeling. *Compos Part B Eng* 80:369–378. <https://doi.org/10.1016/j.compositesb.2015.06.013>
33. Li N, Li Y, Liu S (2016) Rapid prototyping of continuous carbon fiber reinforced polylactic acid composites by 3D printing. *J Mater Process Technol* 238:218–225. <https://doi.org/10.1016/j.jmatprotec.2016.07.025>
34. Hasanzadeh R, Mihankhah P, Azdast T et al (2023) Process-property relationship in polylactic acid composites reinforced by iron microparticles and 3D printed by fused filament fabrication. *Polym Eng Sci*. <https://doi.org/10.1002/pen.26556>
35. Rasouli A, Azdast T, Mohammadzadeh H et al (2022) Morphological properties and mechanical performance of polylactic acid scaffolds fabricated by a novel fused filament fabrication/gas foaming coupled method. *Int J Adv Manuf Technol* 119:7463–7474. <https://doi.org/10.1007/s00170-022-08743-x>
36. Azdast T, Hasanzadeh R (2021) Polylactide scaffold fabrication using a novel combination technique of fused deposition modeling and batch foaming: dimensional accuracy and structural properties. *Int J Adv Manuf Technol* 114:1309–1321. <https://doi.org/10.1007/s00170-021-06915-9>
37. Shah SP, Maiarù M (2021) Effect of manufacturing on the transverse response of polymer matrix composites. *Polymers (Basel)* 13. <https://doi.org/10.3390/polym13152491>
38. Ferretti P, Santi GM, Leon-Cardenas C et al (2021) Representative volume element (RVE) analysis for mechanical characterization of fused deposition modeled components. *Polymers (Basel)* 13. <https://doi.org/10.3390/polym13203555>
39. Aqzna SS, Yeoh CK, Idris M et al (2019) The effect of different raster orientations of ABS - zinc ferrite composites on mechanical, electrical and thermal conductivity properties via 3D printer. *Mater Today: Proc* 16:1804–1808. <https://doi.org/10.1016/j.matpr.2019.06.054>
40. Sa'ude N, Ibrahim M, MHI I (2013) Mechanical properties of highly filled iron-ABS composites in injection molding for FDM wire filament. *MSF* 773-774:448–453. <https://doi.org/10.4028/www.scientific.net/MSF.773-774.448>
41. Mohamed OA, Masood SH, Bhowmik JL (2015) Optimization of fused deposition modeling process parameters: a review of current research and future prospects. *Adv Manuf* 3:42–53. <https://doi.org/10.1007/s40436-014-0097-7>
42. Joanna Izdebska-Podsiadły (2022) *Polymers for 3D printing: Methods, Properties and Characteristics (Plastics Design Library)*. William Andrew Publishing
43. Oksman K, Skrifvars M, Selin J-F (2003) Natural fibres as reinforcement in polylactic acid (PLA) composites. *Compos Sci Technol* 63:1317–1324. [https://doi.org/10.1016/S0266-3538\(03\)00103-9](https://doi.org/10.1016/S0266-3538(03)00103-9)
44. Waheed S, Cabot JM, Smejkal P et al (2019) Three-dimensional printing of abrasive, hard, and thermally conductive synthetic microdiamond-polymer composite using low-cost fused deposition modeling printer. *ACS Appl Mater Interfaces* 11:4353–4363. <https://doi.org/10.1021/acsami.8b18232>
45. dos Santos WN, de Sousa JA, Gregorio R (2013) Thermal conductivity behaviour of polymers around glass transition and crystalline melting temperatures. *Polym Test* 32:987–994. <https://doi.org/10.1016/j.polymertesting.2013.05.007>
46. Bleck W (2016) *Materials science of steel-textbook for students at RWTH. IEHK publishing, Aachen*
47. Goh GD, Yap YL, Agarwala S et al (2019) Recent progress in additive manufacturing of fiber reinforced polymer composite. *Adv Mater Technol* 4:1800271. <https://doi.org/10.1002/admt.201800271>
48. Gebisa AW, Lemu HG (2018) Investigating effects of fused-deposition modeling (FDM) processing parameters on flexural properties of ULTEM 9085 using designed experiment. *Materials (Basel)* 11. <https://doi.org/10.3390/ma11040500>
49. Chicot D, Mendoza J, Zaoui A et al (2011) Mechanical properties of magnetite (Fe<sub>3</sub>O<sub>4</sub>), hematite (α-Fe<sub>2</sub>O<sub>3</sub>) and goethite (α-FeO-OH) by instrumented indentation and molecular dynamics analysis. *Mater Chem Phys* 129:862–870. <https://doi.org/10.1016/j.matchemphys.2011.05.056>
50. Liu Q, Qi F, Wang Q et al (2018) The influence of particles size and its distribution on the degree of stress concentration in particulate reinforced metal matrix composites. *Mater Sci Eng A* 731:351–359. <https://doi.org/10.1016/j.msea.2018.06.067>
51. Chawla N, Chawla KK (2006) Microstructure-based modeling of the deformation behavior of particle reinforced metal matrix composites. *J Mater Sci* 41:913–925. <https://doi.org/10.1007/s10853-006-6572-1>

**Publisher's Note** Springer Nature remains neutral with regard to jurisdictional claims in published maps and institutional affiliations.

Springer Nature or its licensor (e.g. a society or other partner) holds exclusive rights to this article under a publishing agreement with the author(s) or other rightsholder(s); author self-archiving of the accepted manuscript version of this article is solely governed by the terms of such publishing agreement and applicable law.